


Noise-resilient quantum power flow

Fei Feng, Yi-Fan Zhou and Peng Zhang 

ABSTRACT

Quantum power flow (QPF) offers an inspiring direction for overcoming the computation challenge of power flow through quantum computing. However, the practical implementation of existing QPF algorithms in today's noisy-intermediate-scale quantum (NISQ) era remains limited because of their sensitivity to noise. This paper establishes an NISQ-QPF algorithm that enables power flow computation on noisy quantum devices. The main contributions include: (1) a variational quantum circuit (VQC)-based alternating current (AC) power flow formulation, which enables QPF using short-depth quantum circuits; (2) NISQ-compatible QPF solvers based on the variational quantum linear solver (VQLS) and modified fast decoupled power flow; and (3) an error-resilient QPF scheme to relieve the QPF iteration deviations caused by noise; (3) a practical NISQ-QPF framework for implementable and reliable power flow analysis on noisy quantum machines. Extensive simulation tests validate the accuracy and generality of NISQ-QPF for solving practical power flow on IBM's real, noisy quantum computers.

KEYWORDS

Quantum AC power flow, quantum computing, variational quantum linear solver, fast decoupled load flow, noisy-intermediate-scale quantum device.

Power flow is an indispensable foundation for nearly all modern power system analytics, e.g., stochastic power flow, optimal power flow, security screening, transient stability, and reliability assessment^[1-3]. It provides static states of power systems via solving the nodal voltage equations composed of power generation, load, and grid configuration^[4]. The mainstream of alternating current (AC) power flow algorithms consists of the fast-decoupled method, the Newton–Raphson algorithm, the Gauss–Seidel algorithm, etc.^[5] However, under the deep penetration of renewables, an enormous amount of power flow analyses are needed to quantify the impact of uncertainties^[6]. Power flow calculation remains intractable because the complexities of almost all the classical power flow algorithms scale polynomially with the system size.

The fast evolution in quantum computing provides a promising direction for developing scalable power flow analytics^[7-9]. Unlike classical methods, quantum computing enables using logarithmically-scaled number of qubits to solve linear equations in power flow analysis^[10]. A Harrow–Hassidim–Lloyd (HHL)-based quantum power flow (QPF) is devised to underpin the AC power flow issue through quantum computing^[11]. Although the proof-of-concept is successful, the scalability of the method remains limited. The main obstacle is that HHL generates high-depth quantum circuits even for small-scale power flow problems, which can be significantly crippled by noise. Today, noisy-intermediate-scale quantum (NISQ) devices remain to be mainstream, whose capability is restricted by the limited number of qubits and considerable noises^[12]. Noise-tolerant quantum devices may not be available in the near future due to the significant error correction overhead and the short coherence time^[13-15]. Therefore, QPF methods that are applicable to NISQ devices are in high need.

To bridge the gap, this paper devises a NISQ-QPF algorithm that allows for practical and noise-resilient power flow analysis on NISQ devices. Our contributions are as follows:

- A variational quantum circuit (VQC)-based QPF formulation is established to enable QPF analysis using shallow-depth quantum circuits.
- A variational quantum linear solver (VQLS)-QPF solver is devised incorporating power flow information embedding and quantum circuit optimization, which enables resilient quantum power flow iterations under noisy environments.
- VQLS-compatible QPF algorithm is devised by modifying the fast decoupled load flow (FDLF), which tackles the quantum measurement issues of the general VQLS.
- A practical NISQ-QPF framework is constructed for reliable QPF implementation on real quantum computers.

The remainder of this paper is organized as follows: Section 1 establishes the variational quantum power flow formulation. Section 2 develops the variational quantum power flow solver. Section 3 devises the NISQ-compatible QPF algorithm. Section 4 presents extensive case studies on real IBM quantum devices, followed by the conclusion in Section 5.

1 Variational quantum power flow formulation

An indispensable computation burden of nonlinear power flow algorithms is to solve a set of linear equations iteratively, where the required computational resource scales polynomially with the power system scale. This section establishes a variational QPF formulation, which inherits the exponential scalability of quantum computing and enables the utilization of shallow-depth quantum circuits in QPF calculation.

1.1 Classical fast decoupled load flow formulation

FDLF is a widely used derivative-based iterative power flow method for steady-state analysis of power systems. Fixed Jacobian matrices are iteratively used to solve the nonlinear power flow equations based on the strong coupling between voltage magnitudes

V and reactive power Q and between voltage angles θ to active power P ^[16]. According to the operation characteristics of power generation and consumption, the types of buses generally consist of (1) slack bus which supports the power balance of the system; (2) PV bus whose active power and voltage magnitude are fixed; and (3) PQ buses whose active/reactive power are fixed.

Given an N -bus power system with one slack bus, N_{pv} PV buses, and N_{pq} PQ buses, the FDLF models are formulated as^[16]

$$\mathbf{V}^{-1}\Delta\mathbf{P} = \mathbf{B}'\mathbf{V}\Delta\theta \quad (1)$$

$$\mathbf{V}^{-1}\Delta\mathbf{Q} = \mathbf{B}''\Delta\mathbf{V} \quad (2)$$

where $\mathbf{B}' \in \mathbb{R}^{(N-1) \times (N-1)}$ and $\mathbf{B}'' \in \mathbb{R}^{N_{pq} \times N_{pq}}$ are coefficient matrices derived from the admittance matrix; $\Delta\mathbf{V} \in \mathbb{R}^{N_{pq} \times 1}$ and $\Delta\theta \in \mathbb{R}^{(N-1) \times 1}$ are the differences of voltage magnitudes and angles, respectively; $\Delta\mathbf{P} \in \mathbb{R}^{(N-1) \times 1}$ and $\Delta\mathbf{Q} \in \mathbb{R}^{N_{pq} \times 1}$ denote the active/reactive power mismatches, which is updated as

$$\Delta\mathbf{S} = [\Delta\mathbf{P}, \Delta\mathbf{Q}]^T = \mathbf{S} - \bar{\mathbf{Y}}(\theta) \cdot \mathbf{V} \circ \mathbf{V} \quad (3)$$

1.2 VQC-based QPF formulation

The main idea of NISQ-QPF is to establish two separate VQCs to respectively prepare $|\Delta\mathbf{V}\rangle$ and $|\mathbf{V}\Delta\theta\rangle$ according to Eqs. (1) and (2) (here $|\cdot\rangle$ denotes the corresponding quantum state of the original vector¹).

Taking Eq. (2) as an example, we explain the formulation of the fast decoupled, VQC-based QPF. A VQC $U_q(\mathbf{w}_q)$ specified by a set of classical parameters \mathbf{w}_q generates $|\Delta\mathbf{V}\rangle$ as $|\Delta\mathbf{V}\rangle = U_q(\mathbf{w}_q)|0\rangle$. In order to optimize a qualified $U_q(\mathbf{w}_q)$ so that $|\Delta\mathbf{V}\rangle$ provides the solution of Eq. (2), it is required that $\mathbf{B}''|\Delta\mathbf{V}\rangle$ (i.e., the left-hand side of Eq. (2)) is proportional to the normalized quantum state of $\mathbf{V}^{-1}\Delta\mathbf{Q}$ (i.e., the right-hand side of Eq. (2)). Mathematically, the following formulation is established:

$$|\Psi_q\rangle = \frac{\mathbf{B}''|\Delta\mathbf{V}\rangle}{\sqrt{\langle\Delta\mathbf{V}|\mathbf{B}''^T\mathbf{B}''|\Delta\mathbf{V}\rangle}} = |\mathbf{V}^{-1}\Delta\mathbf{Q}\rangle \quad (4)$$

where $|\Psi_q\rangle$ denotes the normalized quantum state of $\mathbf{V}^{-1}\Delta\mathbf{Q}$.

For Eq. (1), the preparation of $|\mathbf{V}\Delta\theta\rangle$ can be devised as the same format of Eq. (4).

$$|\Psi_p\rangle = \frac{\mathbf{B}'|\mathbf{V}\Delta\theta\rangle}{\sqrt{\langle\mathbf{V}\Delta\theta|\mathbf{B}'^T\mathbf{B}'|\mathbf{V}\Delta\theta\rangle}} = |\mathbf{V}^{-1}\Delta\mathbf{P}\rangle \quad (5)$$

where $|\mathbf{V}\Delta\theta\rangle = U_p(\mathbf{w}_p)|0\rangle$ is yielded from another VQC U_p specified by parameters \mathbf{w}_p .

2 Variational quantum power flow solver

This section develops a VQLS-based QPF solver for power flow iterations by optimizing the VQCs.

Figure 1 illustrates the architecture of the VQLS-based QPF algorithm, where a hybrid quantum/classical framework is utilized. The overall idea of this algorithm is the updated power injections $\mathbf{V}^{-1}\Delta\mathbf{P}$ and $\mathbf{V}^{-1}\Delta\mathbf{Q}$ in addition to \mathbf{B}' and \mathbf{B}'' as inputs are sent to VQLS solver. The VQLS-based circuit is then established to obtain the quantum states $|\Delta\mathbf{V}\rangle$ and $|\mathbf{V}\Delta\theta\rangle$. This procedure of VQLS mainly consists of three subroutines namely power flow information updating, VQLS input preparation, and VQC optimization. Detailed procedures of VQLS are as follows:

¹Taking $\Delta\mathbf{V}$ as an example, $|\Delta\mathbf{V}\rangle = \sum_j v_j|j\rangle$, where $v_j = \Delta V_j / \sqrt{\sum_j (\Delta V_j)^2}$; ΔV_j denotes the j -th element of $\Delta\mathbf{V}$; $|j\rangle$ is the j -th quantum basis.

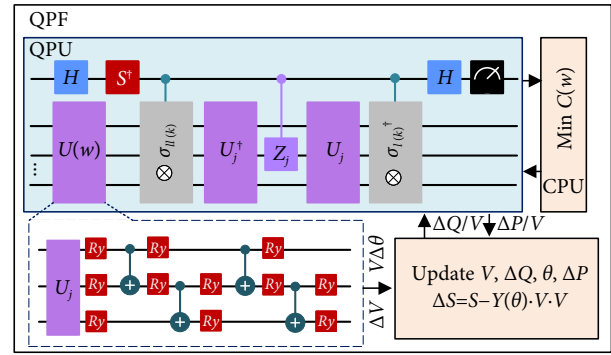


Fig. 1 QPF architecture.

2.1 Power flow information updating

According to Eqs. (1)–(3), the power injections and voltages are updated to obtain $\mathbf{V}^{-1}\Delta\mathbf{P}$ and $\mathbf{V}^{-1}\Delta\mathbf{Q}$ in the CPU, which only involves trivial matrix-vector multiplication.

2.2 VQLS input preparation

The quantum processor unit (QPU) reads the power flow vectors ($\mathbf{V}^{-1}\Delta\mathbf{P}$ and $\mathbf{V}^{-1}\Delta\mathbf{Q}$) and power flow matrices (\mathbf{B}' and \mathbf{B}'') as inputs for the VQLS algorithm to perform linear equation solving in each power flow iteration. Correspondingly, the classical matrices/vectors should be translated into the quantum formulation. To achieve this goal, \mathbf{B}' and \mathbf{B}'' are decomposed into a linear combination of basic Pauli gates^[17]. Take \mathbf{B}'' as an example:

$$\mathbf{B}'' = \sum_{l=1}^{4^n} \frac{1}{2^n} \text{Tr}(\sigma_l \mathbf{B}'') \left(\bigotimes_{k=1}^n \sigma_{l(k)} \right) \quad (6)$$

where n denotes the qubit number; the basic Pauli gate $\sigma_{l(k)}$ on the k -th qubit includes $\{\sigma_I, \sigma_x, \sigma_y, \sigma_z\}$; $\sigma_I = \begin{bmatrix} 1 & 0 \\ 0 & 1 \end{bmatrix}$, $\sigma_x = \begin{bmatrix} 0 & 1 \\ 1 & 0 \end{bmatrix}$, $\sigma_y = \begin{bmatrix} 0 & -i \\ i & 0 \end{bmatrix}$ and $\sigma_z = \begin{bmatrix} 1 & 0 \\ 0 & -1 \end{bmatrix}$ denote the zeroth, Pauli-X,

Pauli-Y, and Pauli-Z mathematical matrices, respectively. $|\mathbf{V}^{-1}\Delta\mathbf{Q}\rangle$ and $|\mathbf{V}^{-1}\Delta\mathbf{P}\rangle$ are decomposed into a basis vector-based formulation so that they can be effectively prepared in the Hilbert space^[18,19].

2.3 VQC optimization for QPF

We establish QPF cost functions to quantify the difference between the normalized states in Eqs. (4) and (5) (i.e., $|\Psi_p\rangle$ and $|\Psi_q\rangle$) and power flow vectors (i.e., $|\mathbf{V}^{-1}\Delta\mathbf{P}\rangle$ and $|\mathbf{V}^{-1}\Delta\mathbf{Q}\rangle$):

$$\mathcal{C}_p = 1 - |\langle \mathbf{V}^{-1}\Delta\mathbf{P} | \Psi_p \rangle|^2, \mathcal{C}_q = 1 - |\langle \mathbf{V}^{-1}\Delta\mathbf{Q} | \Psi_q \rangle|^2 \quad (7)$$

Values of \mathcal{C}_p and \mathcal{C}_q can be estimated by performing a series of Hadamard tests, which is a standard quantum computation technique^[20,21]. For \mathcal{C}_q , specifically, it can be expressed as

$$\mathcal{C}_q = 1 - |\langle \mathbf{V}^{-1}\Delta\mathbf{Q} | \Psi_q \rangle|^2 = 1 - \frac{\sum_{l,l'} r_l r_{l'}^* \langle U^l(\mathbf{w}) \sigma_l^\dagger U_j \mathbf{W} U_j^\dagger \sigma_l U(\mathbf{w}) | \mathbf{0} \rangle}{\sum_{l,l'} r_l r_{l'}^* \langle U^l(\mathbf{w}) \sigma_l^\dagger \sigma_l U(\mathbf{w}) | \mathbf{0} \rangle} \quad (8)$$

where $r_l = \frac{1}{2^n} \text{Tr}(\sigma_l \mathbf{B}'')$ are the decomposition coefficients; \mathbf{W} is a coefficient integrating Pauli-Z gate^[20]. Then, Eq. (7) is minimized to optimize the parameters of the VQCs $U_p(\mathbf{w}_p)$ and $U_q(\mathbf{w}_q)$ ^[22,23]. The subplot in Figure 1 illustrates the VQC architecture designed

for QPF, which is comprised of an initial state encoding layer and several entangling layers^[19]. In detail, a set of Ry quantum gates are installed on each qubit for initial state encoding. An entanglement layer is introduced after the Ry gates to realize the quantum entanglement between adjacent quantum qubits. The entanglement layer can be repeated to achieve the VQC for QPF.

Once the optimization achieves convergence, the maximum overlap can be reached for Eqs. (4) and (5). Then, the possibility of the quantum state $|\Delta V\rangle$ and $|\mathbf{V}\Delta\theta\rangle$ can be measured from the optimized VQCs.

The superiority of the fast-decoupled, VQLS-based QPF lies in three points:

- It embeds power flow equations into the Hilbert space, which only uses logarithmically-scaled computational resources (i.e., number of qubits) to address power flow issues.
- It employs quantum circuits with shallow-depth structures, which are less crippled by noise and, therefore, more compatible with today's real quantum machines.
- It inherits the fixed Jacobian matrix from FDLF so that VQLS only needs to be called at the beginning of the QPF algorithm (rather than at each iteration), which significantly saves the efforts for quantum circuit optimization.

3 NISQ compatible quantum power flow

This section first devises a modified FDLF-based QPF solver to address the practical measurement challenges on real quantum machines.

Next, a practical NISQ-QPF framework is established for reliable power flow analysis. Finally, practical considerations on circuit design and implementation settings are discussed.

3.1 Practical NISQ-QPF algorithm

The aforementioned VQLS-based QPF solver enables obtaining the quantum states of $|\Delta V\rangle$ and $|\mathbf{V}\Delta\theta\rangle$ theoretically. However, the measurement on real quantum machines can only provide probabilities on the quantum basis, i.e., ΔV_j^2 and $(V_j\Delta\theta_j)^2$ rather than ΔV_j and $V_j\Delta\theta_j$ ($\forall j$). The main bottleneck lies in the unknown signs of ΔV_j and $V_j\Delta\theta_j$. Here, we devise practical active/reactive-power-related QPF solvers via modifying FDLF to tackle this challenge.

3.1.1 Active-power-related QPF solver

Rewrite $|\mathbf{V}^{-1}\Delta\mathbf{P}\rangle$ in its basis states as $|\mathbf{V}^{-1}\Delta\mathbf{P}\rangle = \sum v_j|j\rangle$. Correspondingly, the active power flow solution $|\mathbf{V}\Delta\theta\rangle$ can also be described as the linear combination of a set of basis solutions $|\mathbf{V}\Delta\theta\rangle_j$ ($\forall j$).

$$-\mathbf{B}'|\mathbf{V}\Delta\theta\rangle_j = |j\rangle \quad (9)$$

$$|\mathbf{V}\Delta\theta\rangle = \sum_j -v_j|\mathbf{V}\Delta\theta\rangle_j \quad (10)$$

In the FDLF formulation, \mathbf{B}' is constructed by the reciprocal of branch susceptance^[16].

$$B'_{(g,g)} = \sum_{s=1, s \neq g}^N -\frac{1}{x_{(g,s)}}, \quad B'_{(g,m)} = \frac{1}{x_{(g,m)}} \quad (11)$$

where $x_{(g,s)}$ denotes the susceptance of branch (g, m) . Equation (11) shows \mathbf{B}' is a diagonally dominant matrix. Therefore, it can be proved that for an arbitrary j , every element of $|\mathbf{V}\Delta\theta\rangle_j$ is non-negative.

Proof. Assume bus N is the slack bus. Denote $|\mathbf{V}\Delta\theta\rangle_j = [V_1\Delta\theta_1, V_2\Delta\theta_2, \dots, V_g\Delta\theta_g, V_{N-1}\Delta\theta_{N-1}]^T$. Without loss of generality, denote $V_g\Delta\theta_g$ as the smallest element in $\mathbf{V}\Delta\theta$, we prove $V_g\Delta\theta_g \geq 0$ by contradiction.

Assume $V_g\Delta\theta_g < 0$. The g -th dimension of Eq. (9) can be calculated as

$$j_g = \sum_{s=1, s \neq g}^{N-1} \frac{1}{x_{(g,s)}} (V_s\Delta\theta_s - V_g\Delta\theta_g) + \frac{1}{x_{(g,N)}} V_g\Delta\theta_g \quad (12)$$

where $j_g \in \{0, 1\}$ denotes the g -th dimension of $|j\rangle$.

Since $V_g\Delta\theta_g$ is the smallest, $V_s\Delta\theta_s \leq V_g\Delta\theta_g$ for arbitrary s . Meanwhile, since $V_g\Delta\theta_g < 0$, Eq. (12) yields the following conclusion:

$$j_g \leq \sum_{s=1, s \neq g}^{N-1} \frac{1}{x_{(g,s)}} (V_g\Delta\theta_g - V_s\Delta\theta_s) + \frac{1}{x_{(g,N)}} V_g\Delta\theta_g = \frac{1}{x_{(g,N)}} V_g\Delta\theta_g < 0 \quad (13)$$

Formula (13) is in contradiction to the fact that $j_g \in \{0, 1\}$. Therefore, the assumption $V_g\Delta\theta_g < 0$ does not hold and $V_g\Delta\theta_g$ is proved as non-negative.

Consequently, once a VQC is optimized for Eq. (9), the quantum state $|\mathbf{V}\Delta\theta\rangle_j$ (rather than merely the possibility) can be estimated as

$$|\mathbf{V}\Delta\theta\rangle_j = U_{p_j}(\mathbf{w}_{p_j}^n)|\mathbf{0}\rangle = \sum_{k=1}^{2^n} \sqrt{p_k}|k\rangle \quad (14)$$

where p_k denotes the possibility of the k -th basis state, which can be directly measured from real quantum computers.

3.1.2 Reactive-power-related QPF solver

In the FDLF formulation, \mathbf{B}'' is constructed from the imaginary part of the branch and ground admittance. Different from \mathbf{B}' , \mathbf{B}'' does not hold the diagonal dominance characteristic, which therefore hinders the non-negative measurement of the basis solution $|\Delta V\rangle_j$.

Inspired by the instant updating process^[24, 25], a modified $\mathbf{Q} - \mathbf{V}$ iteration is devised to tackle the challenge:

$$\mathbf{V}^{-1}\Delta\mathbf{Q} = \tilde{\mathbf{B}}''\Delta\mathbf{V} + \tilde{\mathbf{B}}''_0\Delta\mathbf{V}_p \quad (15)$$

where $\Delta\mathbf{V}_p$ denotes the differences of voltage magnitude at the previous iteration. Here, we decompose \mathbf{B}'' into a branch admittance related $\tilde{\mathbf{B}}''$ and a ground admittance related $\tilde{\mathbf{B}}''_0$. The detailed elements of $\tilde{\mathbf{B}}''$ and $\tilde{\mathbf{B}}''_0$ include:

$$\tilde{B}''_{(g,g)} = \text{Im}\left(\sum_{s=1, s \neq g}^N y_{(g,s)}\right), \quad \tilde{B}''_{(g,m)} = \text{Im}(-y_{(g,m)}) \quad (16)$$

$$\tilde{B}''_{0(g,g)} = \text{Im}(y_{(g,0)}), \quad \tilde{B}''_{0(g,m)} = 0 \quad (17)$$

where $y_{(g,m)}$ and $y_{(g,0)}$ denotes admittance values of branch (g, m) and ground, respectively, and $\text{Im}(\cdot)$ denotes the imaginary part.

In Eq. (16), the branch admittance related $\tilde{\mathbf{B}}''$ is a diagonally dominant matrix that offers a potential to make $\mathbf{Q} - \mathbf{V}$ iteration compatible to the VQLS-based QPF solver. Rewrite Eq. (15) as a quantum linear formulation format,

$$|\mathbf{V}^{-1}\Delta\mathbf{Q} - \tilde{\mathbf{B}}''_0\Delta\mathbf{V}_p\rangle = \tilde{\mathbf{B}}''|\Delta\mathbf{V}\rangle \quad (18)$$

where $|\mathbf{V}^{-1}\Delta\mathbf{Q} - \tilde{\mathbf{B}}''_0\Delta\mathbf{V}_p\rangle$ can be expressed in its basis states as $|\mathbf{V}^{-1}\Delta\mathbf{Q} - \tilde{\mathbf{B}}''_0\Delta\mathbf{V}_p\rangle = \sum_j v_j|j\rangle$. Detailed proof of the modified $\mathbf{Q} -$

V iteration shares the same way to Eq. (12) and Formula (13).

The modified $Q - V$ iteration retains both the contribution of the ground part and the diagonal dominance characteristic of $\tilde{\mathbf{B}}'$, which therefore enables non-negative measurement of $|\Delta V\rangle$ from Eq. (18).

3.1.3 Augmented QPF solver

Today's quantum computers remain limited qubits for solving linear equations. This motivates us to explore the qubit-economic method which enables fewer quantum resources to solve $P - \theta$ and $Q - V$ iteration at the same time.

Different from the separate calculations for $V\Delta\theta$ and ΔV , an augmented QPF solver is devised to explore the quantum calculation simultaneously by quantum superposition as

$$\begin{bmatrix} \mathbf{B}' & \mathbf{0} \\ \mathbf{0} & \tilde{\mathbf{B}}'' \end{bmatrix} \begin{bmatrix} V\Delta\theta \\ \Delta V \end{bmatrix} = \begin{bmatrix} V^{-1}\Delta P \\ V^{-1}\Delta Q - \tilde{\mathbf{B}}_0''\Delta V_p \end{bmatrix} \quad (19)$$

Compared with the classical method in the Euclidean space scaled by $N_{pq} + N - 1$, and $\lceil \log_2^{N_{pq}} \rceil + \lceil \log_2^{N-1} \rceil$ qubit QPF, the augmented QPF algorithm in Hilbert space only requires $\lceil \log_2^{N_{pq}+N-1} \rceil$ qubits.

3.2 Practical NISQ-QPF framework

A practical NISQ-QPF framework is developed for solving the measurement and noise issues on real quantum computers. Algorithm 1 summarizes the framework and details the pseudo-code of QPF.

3.2.1 Initialization

Power flow information including branch admittance matrices \mathbf{B}' , $\tilde{\mathbf{B}}''$, $\tilde{\mathbf{B}}_0''$, and power data P, Q, θ, V are initialized.

3.2.2 VQLS preparation/optimization

Decompose branch admittance matrices and prepare VQC circuits for obtaining $|\Delta V\rangle$ and $|V\Delta\theta\rangle$ in $P - \theta$ and $Q - V$ iteration. Then, a classical optimizer (i.e., Adam^[26], gradient decent^[27]) is utilized to optimize the parameters of the VQC circuits. When the optimization process is finished, the VQC circuit can be executed on a real quantum machine. Once quantum states of $|V\Delta\theta\rangle$ and $|\Delta V\rangle$ are measured, the corresponding power flow variables θ, V and ΔS can be updated for the next iteration.

3.2.3 Noise error compensation

After the measurement, check the deviations $\xi_{q(0)}$ and $\xi_{p(0)}$. If the deviations are less than the tolerance, V and θ are updated. Otherwise, we perform an iterative error correction of $\Delta V_{(k)}$ and $\Delta\theta_{(k)}$ to relieve the deviations and access the accurate values. Once $\Delta V_{(k)}$ and $\Delta\theta_{(k)}$ reach convergence, V and θ are updated.

The QPF iterations continue until the mismatches ΔP and ΔQ reach a convergence tolerance of ϵ .

3.3 Remarks

Today's NISQ computers are considerably disturbed by noise. To enhance the performance of the devised VQLS-QPF solvers, proper circuit design and operation settings on quantum machines are highly required. Here, the following practical factors are emphasized:

Number of shots. Sufficient quantum shots are required for generating accurate measurements when solving QPF on real quantum devices.

Quantum circuit structure. The real quantum device usually

Algorithm 1. Practical QPF algorithm

```

1 Initialize:  $\theta, V, \mathbf{B}', \tilde{\mathbf{B}}'', \tilde{\mathbf{B}}_0'', P, Q, \epsilon;$ 
while  $\Delta P \geq \epsilon$  or  $\Delta Q \geq \epsilon$  do
2   Update:  $\Delta P, \Delta Q$  Eq. (3);
3   if 1st iteration then
4     Decompose:  $\mathbf{B}', \tilde{\mathbf{B}}'' \Rightarrow \mathbf{B}', \tilde{\mathbf{B}}'';$ 
5     Prepare QPF circuit and  $\mathcal{C}$  Eq. (7)
6     Optimize QPF circuit;
7   end
8   Execute:  $|V^{-1}\Delta P\rangle \xrightarrow{\text{QPF}} |V\Delta\theta\rangle;$ 
9   Execute:  $|V^{-1}\Delta Q - \tilde{\mathbf{B}}_0''\Delta V_p\rangle \xrightarrow{\text{QPF}} |\Delta V\rangle;$ 
10  Check  $\xi_{p(0)}, \xi_{q(0)}$ ;
11  repeat
12    if 1st iteration then
13      Input:  $\Delta\theta \Rightarrow \Delta\theta_{(0)}, \Delta V \Rightarrow \Delta V_{(0)}$ 
14    end
15    Iteratively correct  $\xi_{p(k)}, \Delta\theta_{(k+1)}$  and  $\xi_{q(k)},$ 
       $\Delta V_{(k+1)}$  until convergence
16  until  $\Delta\theta_{(k+1)}$  and  $\Delta V_{(k+1)}$  remain constant;
17  Update:  $\theta, V;$ 
18 end
19 Result:  $\theta, V$  and the branch power flow.

```

only contains several basis gates and provides limited connectivity. If the designed VQC requires nonexistent quantum gates or connection between unconnected qubits, it will be compiled to an equivalent quantum circuit compatible with the hardware availability. Such a compiling process unavoidably increases the depth of the quantum circuit, which may deteriorate the performance of QPF. For instance, if the Pauli-Z gate doesn't exist on real quantum devices, the Hardmard gate and Pauli-X gate are compiled together to realize the function of the nonexistent Pauli-Z gate, which would increase the depth of the quantum circuit.

4 Numerical test

This section validates the effectiveness and accuracy of QPF in a series of standard IEEE test systems. QPF is implemented on an IBM quantum simulator (*IBMQ_qasm_simulator*) with Qiskit (0.16.0)^[28] and a practical quantum machine (*IBMQ_hanoi*).

4.1 Validity of NISQ-QPF on the quantum simulator

This subsection validates the effectiveness of QPF in a typical five-bus test system (see Figure 2) on an IBM quantum simulator. Specifically, bus 5 is a slack bus, bus 1 equipped with a generator, and buses 2, 3, 4 with loads are PQ buses.

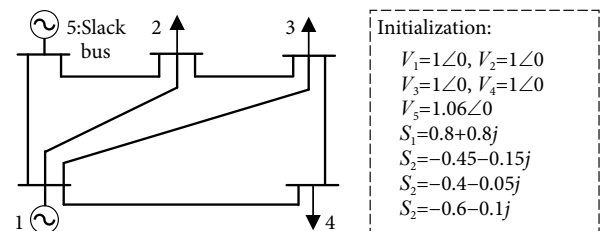


Fig. 2 Five-bus system for QPF tests.

4.1.1 Validation of the NISQ-QPF process

We first exemplify the QPF results on a five-bus test system. 2

qubits are employed to obtain 4 unknown bus voltages. Figure 3 illustrates the optimized QPF quantum circuit and the measurement results for $Q - V$ iteration under one basis state.

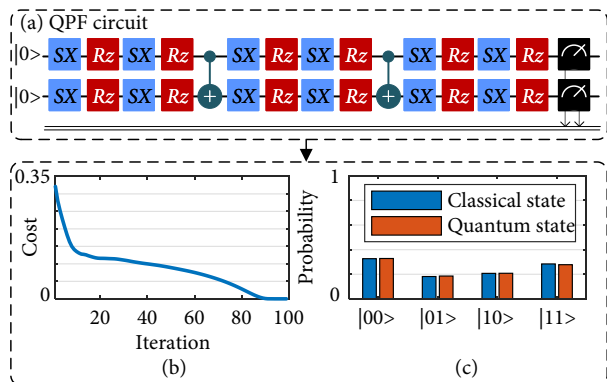


Fig. 3 Demonstration of the QPF process in a five-bus test system. (a) Designed QPF circuit; (b) Optimization process of the cost function for a basis state $V^{-1}\Delta Q = [1, 0, 0, 0]$; (c) Measurement of quantum state.

- The compiled, optimized QPF circuit is presented in Figure 3(a). It is obvious that the circuit is of shallow depth, which is executable on today’s NISQ devices.

- Figure 3(b) provides the evolution of the cost function.

Along the optimization process, the cost function is minimized, which indicates the quantum solution is getting closer to the real solution.

- When the cost function achieves convergence, the quantum states can be measured from the optimized circuit. Figure 3(c) illustrates the perfect match between the measured quantum solutions and the classical power flow solutions, which validates the accuracy of the VQLS-based QPF solver.

4.1.2 Comparison with classical results

QPF’s correctness and convergence are validated by comparing QPF results against those from classical power flow methods (i.e., FDLF and Newton power flow (NTPF)).

- Table 1 presents the voltage profiles of buses 2 and 3 under different power flow methods. It illustrates the QPF results are identical to the classical results, which validates the correctness of QPF.

- We further study the performance of QPF under a stressed condition, where the loads on buses 3 and 4 are significantly increased to $-1 - 1j$ p.u. and $-1.6 - 1j$ p.u. Figure 4 presents the simulation result. It can be observed that the power flow solution of QPF is still identical to that of the classical method. Although the iteration number increases to 40 because the system is approaching the noise point, QPF still presents satisfactory and comparable convergence performance against classical power flow methods, i.e., the iteration number of QPF is nearly the same as that of the classical methods.

4.1.3 Comparison with HHL-QPF

The devised QPF method is more compatible than HHL-QPF [11] on today’s real, noisy quantum devices. For example, in the five-bus test system, the depth of the compiled circuit optimized from the devised NISQ-QPF algorithm is 15, which is smaller than that of the HHL-QPF method (i.e., 14,811) on the same quantum basis. This indicates the NISQ-QPF method can significantly relieve the impact of noisy quantum environments.

Table 1 Voltage profiles with different methods (p.u.).

Algorithm	Iter	V_1	V_2	θ_1	θ_2
QPF	1	1.0921	1.0708	-0.0041	-0.0580
	2	1.0821	1.0419	-0.0304	-0.0738
	3	1.0734	1.0357	-0.0286	-0.0675
	4	1.0750	1.0390	-0.0264	-0.0663
	5	1.0756	1.0394	-0.0268	-0.0670
	6	1.0755	1.0392	-0.0268	-0.0670
	7	1.0755	1.0392	-0.0268	-0.0670
FDLF	1	1.0912	1.0686	-0.0032	-0.0603
	2	1.0822	1.0398	-0.0305	-0.0732
	3	1.0733	1.0360	-0.0287	-0.0667
	4	1.0750	1.0395	-0.0262	-0.0663
	5	1.0757	1.0394	-0.0266	-0.0670
	6	1.0755	1.0391	-0.0268	-0.0670
	7	1.0755	1.0392	-0.0268	-0.0670
NTPF	1	1.0859	1.0479	-0.0282	-0.0722
	2	1.0757	1.0393	-0.0268	-0.0670
	3	1.0755	1.0392	-0.0268	-0.0670

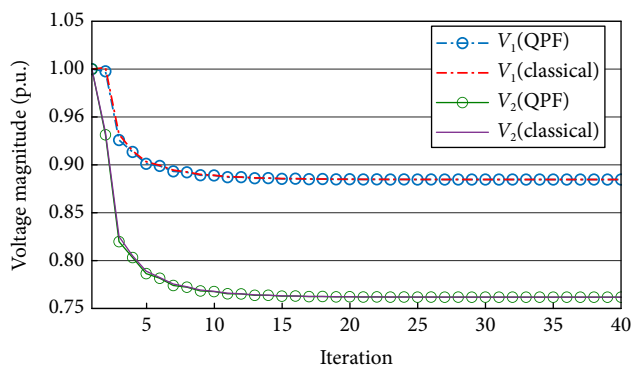


Fig. 4 Voltage profiles under the stressed condition

4.2 NISQ-QPF test on noisy quantum machine

This subsection further verifies the performance of NISQ-QPF using the nine-bus test system [29] in Figure 5 on a real IBM quantum hardware *IBMQ_hanoi*. *IBMQ_hanoi* is a 27-qubit, 64-quantum volume quantum computer, whose median CNOT error is 9.72×10^{-3} and median readout error is 1.31×10^{-2} (see Figure 6 for its configuration). The number of quantum shots is set as 8192.

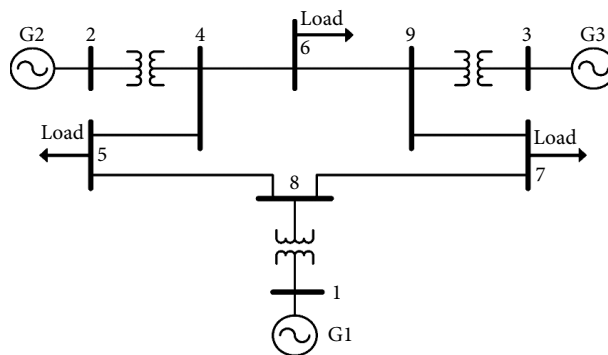


Fig. 5 9-bus system architecture.

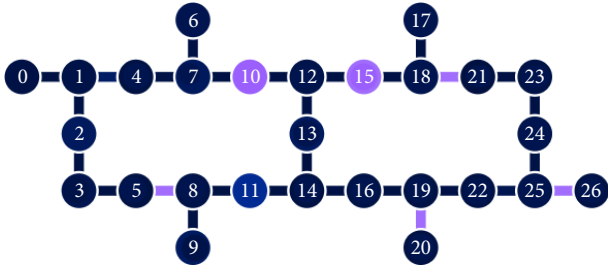


Fig. 6 IBMQ-hanoi configuration.

4.2.1 Performance of NISQ-QPF on IBMQ_hanoi

Figure 7 presents the optimized QPF circuit for a single iteration in the power flow calculation of the nine-bus test system. Detailed quantum gates are shown in Appendix A. It can be observed that

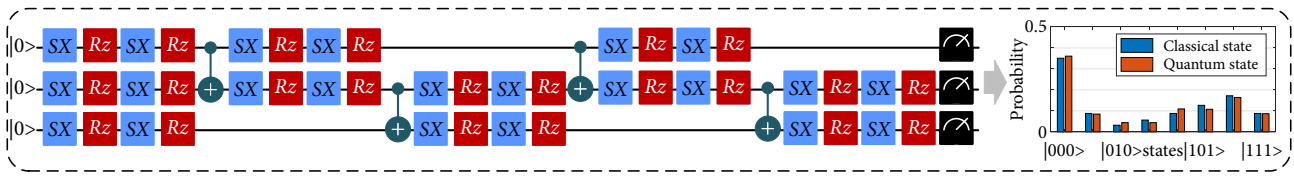


Fig. 7 QPF circuit of the 9-bus test system and its output on real quantum machine.

Table 2 Voltage profiles of the 9-bus system with different methods.

Bus	V_{quantum}	$V_{\text{classical}}$	θ_{quantum}	$\theta_{\text{classical}}$
1	1.0400	1.0400	0.0000	0.0000
2	1.0250	1.0250	0.0814	0.0814
3	1.0250	1.0250	0.1620	0.1620
4	1.0324	1.0324	0.0343	0.0343
5	1.0127	1.0127	-0.0644	-0.0644
6	1.0159	1.0159	0.0127	0.0127
7	0.9956	0.9956	-0.0696	-0.0696
8	1.0258	1.0258	-0.0387	-0.0387
9	1.0258	1.0258	0.0649	0.0649
Er(%)	0.0025		0.0019	

4.2.2 Extension to stochastic QPF analysis

The devised QPF method is extended to the stochastic power flow analysis. Assuming that power injections at buses 5 and 6 follow correlated Gaussian probability distributions (correlation coefficient: 0.75), 5000 samples are generated stochastically. Figure 8 shows the correlation distributions and probability distributions of voltage magnitudes at buses 5 and 6 obtained from the NISQ-QPF. Therefore, NISQ-QPF also provides a promising tool for stochastic power flow analysis.

4.3 Scalability analysis of NISQ-QPF

This subsection explores the performance of the NISQ-QPF method in different scaled practical systems. The scale of the test system is increased from 5 to 9, 30, and 118 bus systems in Figure 9, respectively.

Table 3 presents partial voltage profiles obtained from the real quantum computer, in which V_q and θ_q are QPF voltages, V_c and θ_c are FDLF voltages. Table 4 quantifies QPF’s iteration performance and accuracy compared with the classical method. Some insights can be observed as follows:

- Table 3 illustrates the generality of QPF in the application of

the NISQ-QPF leads to a shallow circuit depth and fewer CNOT gates. While NISQ-QPF only employs 4 CNOT gates in a 24-depth circuit, HHL-QPF requires a 15,795-depth circuit and 54,004 CNOT gates for the same system. Therefore, NISQ-QPF is more scalable than HHL-QPF. More importantly, the shallow-depth quantum circuit is significantly more noise-resilient. As shown in Figure 7, there only exist slight differences between the measurements from the real quantum hardware and the classical solutions, which indicates NISQ-QPF maintains high performance even on today’s noisy machines.

Meanwhile, Table 2 presents the voltage profiles under different methods. It can be observed that QPF results obtained from real quantum hardware are identical to those from the classical methods. Therefore, although noises perturb the quantum solutions, QPF remains to achieve convergence and provide high-fidelity power flow solutions.

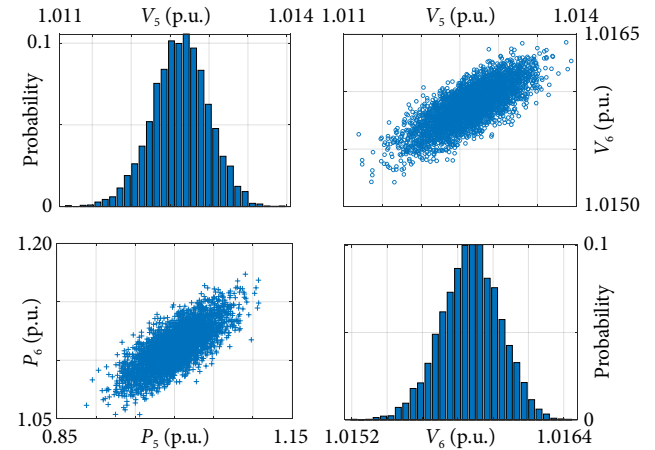


Fig. 8 Probabilistic voltages at buses 5 and 6 and their correlations; (a) Probabilistic voltages at bus 5; (b) The correlation of voltages between buses 5 and 6; (c) The correlation of power injections between buses 5 and 6; (d) Probabilistic voltages at bus 6.

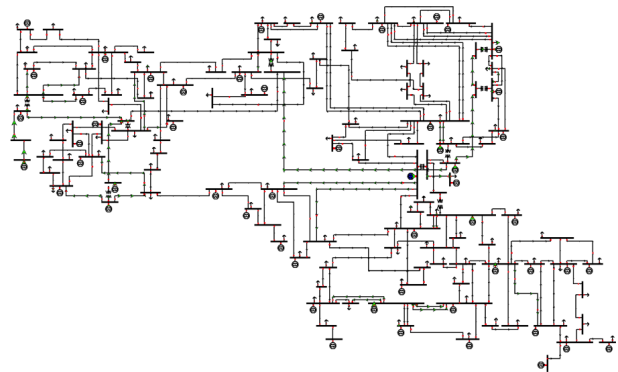


Fig. 9 118-bus system architecture.

practical power systems. For example, the 9-bus test case includes the majority of power components such as the branch, transformer, ground admittance, etc.

Table 3 Partial QPF voltage profiles in different systems.

System	Bus	V_q	V_c	θ_q	θ_c
5-bus	1	1.0755	1.0755	-0.0268	-0.0268
	2	1.0391	1.0391	-0.0669	-0.0669
	3	1.0396	1.0396	-0.0713	-0.0713
	4	1.0393	1.0393	-0.0823	-0.0823
	5	1.0127	1.0127	-0.0644	-0.0644
9-bus	6	1.0324	1.0324	0.0343	0.0343
	7	1.0159	1.0159	0.0127	0.0127
	8	1.0258	1.0258	0.0649	0.0649
	20	0.9692	0.9692	-0.0676	-0.0676
	21	0.9934	0.9934	-0.0609	-0.0609
30-bus	22	1.0000	1.0000	-0.0592	-0.0592
	23	1.0000	1.0000	-0.0277	-0.0277
	24	0.9886	0.9886	-0.0459	-0.0459
	25	0.9902	0.9902	-0.0295	-0.0295
	100	1.0170	1.0170	0.4897	0.4897
118-bus	101	0.9914	0.9914	0.5174	0.5174
	102	0.9891	0.9891	0.5649	0.5649
	103	1.0100	1.0100	0.4244	0.4244
	104	0.9710	0.9710	0.3796	0.3796
	105	0.9650	0.9650	0.3603	0.3603

• The scalability of QPF is validated via different scales of test systems. For example, as shown in Table 3, the voltage magnitude (i.e., 1.0170 p.u.) and angle (0.4897 p.u.) of bus 100 via QPF in the 118-bus system are identical to those of the classical method. Meanwhile, the accuracy is further verified by comparing the mean absolute error (MAE) and root-mean-square error (RMSE) in Table 4. For example, the MAE and RMSE of voltage angles in the 118-bus system are 2.31×10^{-8} p.u. and 5.34×10^{-8} p.u., which satisfy the accuracy requirements.

Table 4 QPF convergence/accuracy in different systems.

System	Accuracy	Iter		MAE (10^{-6} p.u.)	RMSE (10^{-6} p.u.)
		QPF	Classical		
5-bus	$P - \theta$	3	3	0	0
	$Q - V$	3	3	0	0
9-bus	$P - \theta$	4	4	0	0
	$Q - V$	3	3	0	0
30-bus	$P - \theta$	7	6	0	0
	$Q - V$	6	6	0	0
118-bus	$P - \theta$	4	3	0.0231	0.0534
	$Q - V$	3	3	1.0747	1.3954

• Table 4 validates the satisfying iteration performance of QPF. For example, the $Q - V$ iteration number of QPF in the 118-bus system is 3, which is the same as that of the classical one.

It is not that today's quantum computers still have limited capability for solving the quantum power flow, for example, the accessible maximum qubits of IBM quantum devices *IBMQ_washington* are 127 which is one of the obstacles to extending the scalability of quantum computing. Meanwhile, the ideal noise-free quantum computers are not available yet within near decades to

support the high-volume quantum depth circuit. The main bottlenecks lie in large error correction overhead, limited topology connections among quantum qubits, and short coherence time. Quantum computers are required to calculate power flow repeatedly for highly accurate solutions which leads to expensive time consumption. The good news is that enhanced quantum devices with more accuracy and qubits will be developed in the near future such as the 1000-plus-qubit quantum computer^[30]. The swift development of quantum computers offers promising direction to support the quantum algorithm in near future.

5 Conclusion

This paper devises a NISQ-compatible QPF algorithm. Compared with our previous HHL-QPF method, the devised QPF method enables practical and scalable power flow analysis using shallow-depth quantum circuits on real quantum machines. Case studies validate the accuracy and generality of QPF on a quantum simulator and a real IBM quantum machine *IBMQ_hanoi*. NISQ-QPF lays a solid foundation for power system static analytics and energy management through quantum computing in today's NISQ era.

Appendix

A Quantum gates in the paper

In the QPF quantum circuit, \sqrt{X} (or SX) is the squared X gate^[31], which can be expressed as

$$\sqrt{X} = \frac{1}{2} \begin{bmatrix} 1+i & 1-i \\ 1-i & 1+i \end{bmatrix}$$

R_z denotes the single-qubit rotation gate about the Z -axis, which can be formulated as

$$R_z(\theta) = \begin{bmatrix} e^{-i\theta/2} & 0 \\ 0 & e^{i\theta/2} \end{bmatrix}$$

CNOT (or CX) denotes the controlled NOT gate, whose representation is

$$\text{CNOT} = \begin{bmatrix} 1 & 0 & 0 & 0 \\ 0 & 1 & 0 & 0 \\ 0 & 0 & 0 & 1 \\ 0 & 0 & 1 & 0 \end{bmatrix}$$

Acknowledgements

This work is based upon work supported in part by the U.S. Department of Energy's Office of Energy Efficiency and Renewable Energy (EERE) Solar Energy Technologies Office Award (No. 38456), and in part by the National Science Foundation (No. OIA-2134840). Any opinions, findings, and conclusions, or recommendations expressed herein do not necessarily represent the views of the Department of Energy, the National Science Foundation, or the United States Government.

Article history

Received: 11 March 2023; Revised: 5 April 2023; Accepted: 12 April 2023

Additional information

© 2023 The Author(s). This is an open access article under the CC BY license (<http://creativecommons.org/licenses/by/4.0/>).

Declaration of competing interest

The authors have no competing interests to declare that are relevant to the content of this article.

References

- [1] Feng, F., Zhang, P. (2020). Enhanced microgrid power flow incorporating hierarchical control. *IEEE Transactions on Power Systems*, 35: 2463–2466.
- [2] Wang, Y., Zhong, H., Xia, Q., Kirschen, D. S., Kang C. (2016). An approach for integrated generation and transmission maintenance scheduling considering N-1 contingencies. *IEEE Transactions on Power Systems*, 31: 2225–2233.
- [3] Yang, Y., Yang, Z., Yu, J., Zhang, B., Zhang, Y., Yu, H. (2020). Fast calculation of probabilistic power flow: A model-based deep learning approach. *IEEE Transactions on Smart Grid*, 11: 2235–2244.
- [4] Feng, F., Zhang, P., Zhou, Y., Wang, L. (2023). Distributed networked microgrids power flow. *IEEE Transactions on Power Systems*, 38: 1405–1419.
- [5] Dommel, H. W. (1975). Analysis of large power systems. Available at: <https://ntrs.nasa.gov/api/citations/19750021777/downloads/19750021777.pdf>.
- [6] Ren, Z., Li, W., Billinton, R., Yan, W. (2016). Probabilistic power flow analysis based on the stochastic response surface method. *IEEE Transactions on Power Systems*, 31: 2307–2315.
- [7] Zhou, Y., Tang, Z., Nikmehr, N., Babahajiani, P., Feng, F., Wei, T. C., Zheng, H., Zhang, P. (2022). Quantum computing in power systems. *iEnergy*, 1: 170–187.
- [8] Chen, C. C., Shiau, S. Y., Wu, M.F., Wu, Y. R. (2019). Hybrid classical-quantum linear solver using Noisy Intermediate-Scale Quantum machines. *Scientific Reports*, 9: 16251.
- [9] Zhou, Y., Feng, F., Zhang, P. (2021). Quantum electromagnetic transients program. *IEEE Transactions on Power Systems*, 36: 3813–3816.
- [10] Berry, D. W., Childs, A. M., Ostrander, A., Wang, G. (2017). Quantum algorithm for linear differential equations with exponentially improved dependence on precision. *Communications in Mathematical Physics*, 356: 1057–1081.
- [11] Feng, F., Zhou, Y., Zhang, P. (2021). Quantum power flow. *IEEE Transactions on Power Systems*, 36: 3810–3812.
- [12] Dervovic, D., Herbst, M., Mountney, P., Severini, S., Usher, N., Wossnig, L. (2018). Quantum linear systems algorithms: A primer. *arXiv preprint*: 1802.08227.
- [13] Nielsen, M. A., Chuang, I. L. (2012). Quantum Computation and Quantum Information. Cambridge, UK: Cambridge University Press.
- [14] Feng, F., Zhang, P., Zhou, Y., Tang, Z. (2022). Quantum microgrid state estimation. *Electric Power Systems Research*, 212: 108386.
- [15] Cerezo, M., Arrasmith, A., Babbush, R., Benjamin, S. C., Endo, S., Fujii, K., McClean, J. R., Mitarai, K., Yuan, X., Cincio, L., Coles, P. J. (2021). Variational quantum algorithms. *Nature Reviews Physics*, 3: 625–644.
- [16] Stott, B., Alsac, O. (1974). Fast decoupled load flow. *IEEE Transactions on Power Apparatus and Systems*, PAS-93: 859–869.
- [17] Brown, A. R., Susskind, L. (2018). Second law of quantum complexity. *Physical Review D*, 97: 086015.
- [18] Córcoles, A. D., Takita, M., Inoue, K., Lekuch, S., Mineev, Z. K., Chow, J. M., Gambetta, J. M. (2021). Exploiting dynamic quantum circuits in a quantum algorithm with superconducting qubits. *Physical Review Letters*, 127: 100501.
- [19] Zhou, Y., Zhang, P., Feng, F. (2023). Noisy-intermediate-scale quantum electromagnetic transients program. *IEEE Transactions on Power Systems*, 38: 1558–1571.
- [20] Bravo-Prieto, C., LaRose, R., Cerezo, M., Subasi, Y., Cincio, L., Coles, P. J. (2020). Variational quantum linear solver: A hybrid algorithm for linear systems. *Bulletin of the American Physical Society*, 65: F07.00005.
- [21] Aharonov, D., Jones, V., Landau, Z. (2006). A polynomial quantum algorithm for approximating the Jones polynomial. In: Proceedings of the thirty-eighth annual ACM symposium on Theory of Computing, Seattle, WA, USA.
- [22] Kandala, A., Mezzacapo, A., Temme, K., Takita, M., Brink, M., Chow, J. M., Gambetta, J. M. (2017). Hardware-efficient variational quantum eigensolver for small molecules and quantum magnets. *Nature*, 549: 242–246.
- [23] Mitarai, K., Negoro, M., Kitagawa, M., Fujii, K. (2018). Quantum circuit learning. *Physical Review A*, 98: 032309.
- [24] Zimmerman, R. (1996). Comprehensive distribution power flow: Modeling, formulation, solution algorithms and analysis. PhD thesis, Cornell University, Ithaca, NY, USA.
- [25] Feng, F., Zhang, P. (2020). Implicit Z_{bus} Gauss algorithm revisited. *IEEE Transactions on Power Systems*, 35: 4108–4111.
- [26] Kingma, D. P., Ba, J. (2014). Adam: A method for stochastic optimization. *arXiv preprint*: 1412.6980.
- [27] Ruder, S. (2016). An overview of gradient descent optimization algorithms. *arXiv preprint*: 1609.04747.
- [28] Wille, R., Van Meter, R., Naveh, (2019). Y. IBM's Qiskit tool chain: Working with and developing for real quantum computers. In: Proceedings of the 2019 Design, Automation & Test in Europe Conference & Exhibition (DATE), Florence, Italy.
- [29] Shekar, M. C., Aarthi, N. (2018). Contingency analysis of IEEE 9 bus system. In: Proceedings of the 2018 3rd IEEE International Conference on Recent Trends in Electronics, Information & Communication Technology (RTEICT), Bangalore, India.
- [30] (2020). IBM promises 1000-qubit quantum computer—a milestone—by 2023. Available at: <https://doi.org/10.1126/science.abe8122>.
- [31] Feng, F., Zhang, P., Bragin, M. A., Zhou, Y. (2022). Novel resolution of unit commitment problems through quantum surrogate Lagrangian relaxation. *IEEE Transactions on Power Systems*, <https://doi.org/10.1109/TPWRS.2022.3181221>.